

Adsorption, Wetting, Growth, and Thermal Stability of the Protic Ionic Liquid Diethylmethylammonium Trifluoromethanesulfonate on Ag(111) and Au(111)

Stephen Massicot, Tomoya Sasaki, Matthias Lexow, Sunghwan Shin, Florian Maier, Susumu Kuwabata, and Hans-Peter Steinrück*



Cite This: *Langmuir* 2021, 37, 11552–11560



Read Online

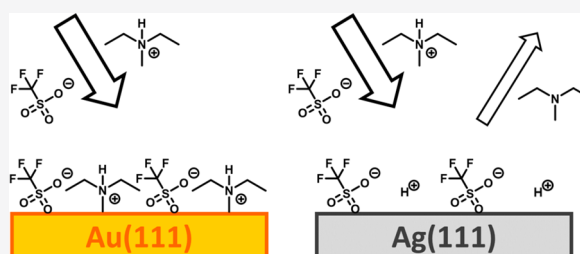
ACCESS |

Metrics & More

Article Recommendations

Supporting Information

ABSTRACT: We have studied the adsorption, wetting, growth, and thermal evolution of the protic IL diethylmethylammonium trifluoromethanesulfonate ([dema][TfO]) on Au(111) and Ag(111). Ultrathin films were deposited at room temperature (RT) and at 90 K, and were characterized *in situ* by angle-resolved X-ray photoelectron spectroscopy. For both surfaces, we observe that independent of temperature, initially, a closed 2D wetting layer forms. While the film thickness does not increase past this wetting layer at RT, at 200 K and below, “moderate” 3D island growth occurs on top of the wetting layer. Upon heating, on Au(111), the [dema][TfO] multilayers desorb at 292 K, leaving an intact [dema][TfO] wetting layer, which desorbs intact at 348 K. The behavior on Ag(111) is much more complex. Upon heating [dema][TfO] deposited at 90 K, the [dema]⁺ cations deprotonate in two steps at 185 and 305 K, yielding H[TfO] and volatile [dema]⁰. At 355 K, the formed H[TfO] wetting layer partly desorbs (~50%) and partly decomposes to form an F-containing surface species, which is stable up to 570 K.



INTRODUCTION

Ionic liquids (ILs) are salts that are composed of poorly coordinating ions and thus exhibit melting points typically well below 100 °C. An interesting, but hitherto not much studied subset of ILs are protic ionic liquids (PILs), which are prepared through the stoichiometric neutralization of a strong Brønsted acid with a strong Brønsted base.¹ This simple synthetic pathway makes them much cheaper than aprotic ionic liquids (AILs) and hence suitable for large-scale commercial applications.^{2,3} One further key feature, in contrast to AILs, is the proton availability for transfer reactions due to the presence of proton donor/proton acceptor sites. This property also allows for the formation of extensive hydrogen bond networks⁴ and makes PILs promising candidates as electrolytes in fuel cells and in catalysis.^{1,4–10} The PIL addressed in the present investigation, diethylmethylammonium trifluoromethanesulfonate, [dema][TfO] (Figure 1), e.g., enables reliable O₂ reduction conditions due to its high and stable open-circuit potential combined with a wide liquid temperature range and high thermal stability.¹⁰

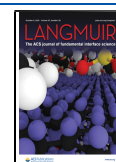
As fuel cells and catalysts usually are operated at elevated temperature, high thermal stability of the PIL at the interface of the electrode and catalyst material is of upmost interest.^{5–7,9,10} In the present work, we characterize in detail the interface formed by [dema][TfO] with Au(111) and Ag(111) as model metal substrates. We investigated the temperature dependent stability of the PIL on both substrates.

On gold, the PIL remains intact; however, on silver, it deprotonates and partially decomposes. For future applications, these differences show the importance of choosing suitable PIL and electrode/catalyst material combinations.

Information on the adsorption, wetting, and growth of PILs on solid substrates also is highly relevant for applications like nanofabrication. On the basis of the very low vapor pressure of ILs in general,^{11,12} stable nanodroplets of PILs on solid supports have recently been used for templating nanostructures.^{13,14} This is not possible with conventional molecular liquids due to their typically finite vapor pressure.¹⁴ Fundamental knowledge on the PIL/solid interaction and wetting characteristics is essential for understanding and tailoring the formation of such nanodroplets, and for rationalizing the sometimes unexpected interfacial properties of PILs.⁵ Other interesting applications are heterogeneous metal catalysis using PILs,^{15,16} batteries with PIL electrolyte,^{17,18} biomass processing with PILs,^{19,20} hydrogen storage

Received: July 8, 2021

Published: September 27, 2021



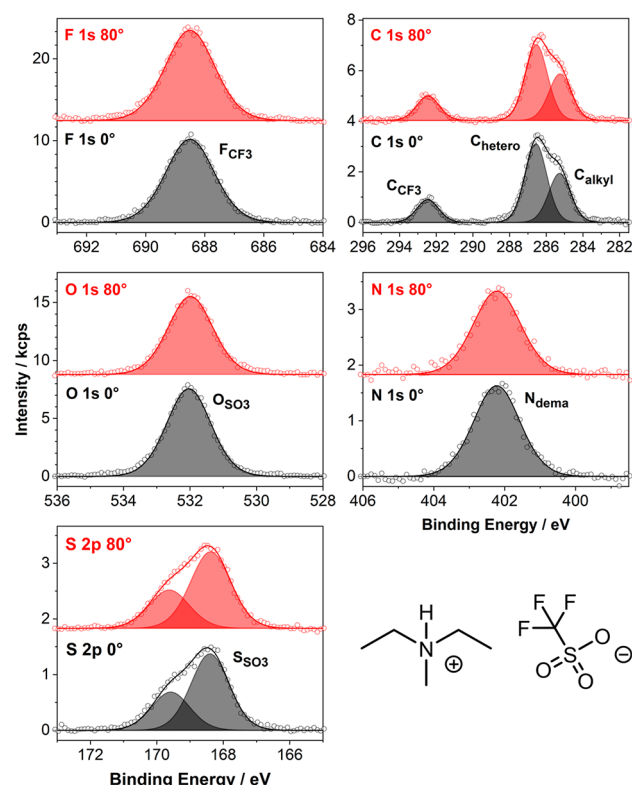


Figure 1. F 1s, C 1s, O 1s, N 1s, and S 2p XP spectra of a macroscopic film of [dema][TfO] on a Ag foil at RT, collected at 0° (black) and 80° (red) emission. At the right bottom, the molecular structure of diethylmethylammonium trifluoromethanesulfonate, [dema][TfO], is shown.

in palladium in PIL electrolyte,²¹ and metal nanoparticle synthesis in PILs.^{22–27}

The goal of this study thus is the detailed characterization of the PIL/support interface. Such information is presently not available. In the past, we already acquired extensive knowledge on interfacial characteristics of ultrathin AIL films on single crystal surfaces under well-defined ultrahigh vacuum (UHV) conditions (see, e.g., recent comprehensive review by Lexow et al.²⁸). This paper is to the best of our knowledge the first work addressing ultrathin PIL films under similar conditions.

We have chosen the above-mentioned PIL [dema][TfO] due to its melting point below RT (260–267 K),^{5,10} its high thermal stability (decomposition at ~630 K),^{5,10} and its equilibrium very far on the ionic side (ΔpK_a well above 17^{5,7,29}). Moreover, the electronic structure of macroscopic samples of [dema][TfO] has already been studied by X-ray photoelectron spectroscopy (XPS),^{30–32} proving the stability

of this PIL under UHV and serving as references for our analysis.

We investigate ultrathin films of [dema][TfO] from submonolayer coverage up to several nanometer thickness, which are deposited by physical vapor deposition (PVD) on Ag(111) and Au(111) at temperatures between 90 and 300 K; PVD allows for the preparation of ultraclean IL films of variable thickness under ultrahigh vacuum conditions.^{28,33} The experiments are performed by angle-resolved X-ray photoelectron spectroscopy (ARXPS). By measuring different electron emission angles of 0° and 80° with respect to the surface normal, we can tune our measurements from bulk-sensitive to surface-sensitive, respectively. Using Al K α radiation, the information depth (ID) at 0° is 7–9 nm, depending on the kinetic energy. At 80°, the ID is 1–1.5 nm, which means that only the outermost surface layers are probed. For bulk ILs, ARXPS thus allows for extracting information on molecular orientation and enrichment effects at the IL/vacuum interface, and for ultrathin IL films, it provides access to the initial adsorption steps, molecular orientation, film growth, and decomposition effects.³⁴ The two noble metal substrates Ag(111) and Au(111) were selected due to their overall low reactivity in general and with ultrathin AIL films in particular. For both, no reactions with metal atoms or reconstruction effects upon AIL deposition were found in previous studies.^{28,35} Nevertheless, Ag is known to be more reactive than Au, e.g., it acts as heterogeneous catalyst for activating molecular oxygen in coupling reactions.^{36,37} By covering temperatures up to 600 K, we also address the desorption of [dema][TfO] multilayers and wetting layers with a focus on adsorption strength, film stability, and thermal decomposition. ARXPS data collected from macroscopic [dema][TfO] samples are used as reference for our thin film studies. This work provides the beginning for PIL/metal interface investigations on the molecular level and will serve as a basis for studies on more reactive PIL/support combinations.

RESULTS AND DISCUSSION

Macroscopic [dema][TfO] Film. We start with addressing a macroscopic [dema][TfO] film with around 0.1 mm thickness that was prepared *ex situ* by spreading the PIL on a polycrystalline Ag foil. At this film thickness, no influence of the substrate is expected. The corresponding ARXP spectra, taken at room temperature (RT), allow for verifying the purity of the PIL and serve as a reference system for comparison with the ultrathin films studied below.

Figure 1 shows F 1s, C 1s, O 1s, N 1s, and S 2p spectra for emission angles of 0° (normal emission, black) and 80° (grazing emission, red) along with their fits (for details, see the [Experimental Section](#)). The [dema]⁺ cation displays two

Table 1. Film Composition as Determined from by XPS in Normal Emission (0°, top) and Grazing Emission (80°, bottom)^a

0°	C _{CF3}	C _{hetero}	C _{alkyl}	N _{dema}	F _{CF3}	O _{SO3}	S _{SO3}
atom number	0.9 / 0.9 (1)	3.1 / 3.1 (3)	2.1 / 2.0 (2)	0.9 / 1.1 (1)	3.2 / 3.0 (3)	3.0 / 3.0 (3)	0.9 / 1.0 (1)
BE/eV	293.0/292.5	286.9/286.6	285.6/ 285.3	402.5/402.2	689.1/ 688.5	532.6/ 532.0	168.9/168.4
80°	C _{CF3}	C _{hetero}	C _{alkyl}	N _{dema}	F _{CF3}	O _{SO3}	S _{SO3}
atom number	1.0 / 1.0 (1)	3.2 / 3.1 (3)	2.1 / 1.9 (2)	0.9 / 1.0 (1)	3.2 / 3.3 (3)	2.6 / 2.7 (3)	1.0 / 1.1 (1)
BE/eV	293.1/292.5	287.0/286.5	285.8/285.2	402.6/ 402.2	689.2/ 688.5	532.8/ 532.0	169.1 / 168.4

^aAlso denoted are the corresponding binding energies. The **bold** values (left) corresponds to a 2.6 nm thick film of [dema][TfO] on Ag(111) at 90 K prepared by PVD, the *italic* values (right) to a macroscopic droplet of ~0.1 mm thickness at RT; the nominal composition in atom numbers are given in (brackets). For S 2p, the binding energy (BE) of the S 2p_{3/2} peak is given; the S 2p_{1/2} peak is at 1.18 eV higher BE.

distinct signals in the C 1s and one in the N 1s region. The C_{hetero} peak at 286.6 eV binding energy (BE) is assigned to the three carbon atoms in direct contact with the nitrogen (hetero) atom and the C_{alkyl} peak at 285.3 eV is assigned to the two alkyl carbon atoms at the end of the ethyl groups. The $C_{\text{alkyl}}:C_{\text{hetero}}$ ratio of 3.1:2.0 at 0° emission is in excellent agreement with the nominal ratio of 3:2. The single N_{dema} peak at 402.2 eV corresponds to the ammonium nitrogen atom.^{30–32} For the $[\text{TfO}]^-$ anion, we observe one peak each in the C 1s, F 1s, and O 1s region. The C_{CF_3} peak at 292.5 eV and the F_{CF_3} peak at 688.5 eV are assigned to carbon and fluorine atoms of the trifluoromethyl group, and the O_{SO_3} peak at 532.0 eV and the spin orbit-split $2p_{3/2}/2p_{1/2}$ S_{SO_3} doublet at 168.4/169.6 eV are assigned to the oxygen and sulfur atoms of the sulfonate group.^{30–32}

The quantitative analysis of the XP spectra of the macroscopic $[\text{dema}][\text{TfO}]$ film is summarized in Table 1. For the bulk-sensitive spectra at 0° , the measured atom numbers obtained from the intensities of the different peaks (right value, italics) show excellent agreement with the nominal values (in brackets), within the accuracy of our measurements ($\pm 5\%$). For the $\sim 6\times$ more surface-sensitive spectra at 80° , the F 1s signal is higher than the nominal value (3.3 vs. 3.0), whereas the O 1s signal is lower than the nominal value (2.7 vs. 3.0). We interpret this observation as an enrichment effect based on preferential orientation of the $[\text{TfO}]^-$ anion at the outer surface with the CF_3 groups pointing toward the vacuum and the SO_3 groups toward the bulk.¹³ A similar preferential enrichment at the IL/vacuum interface was reported also for AILs with CF_3 -containing anions such as bis[(trifluoromethyl)sulfonyl]imide^{13,38} and cations like 3-methyl-1-(3,3,4,4,4-pentafluorobutyl)-imidazolium.^{13,39,40}

As will be demonstrated in the following sections, multilayer desorption, that is, evaporation of the $[\text{dema}][\text{TfO}]$ film already starts around 290 K, which indicates that macroscopic films are not fully stable at RT under UHV conditions. Notably, the evaporation temperature of this protic IL is lower than those of aprotic ILs (e.g., 345 K for $[\text{C}_1\text{C}_1\text{Im}][\text{Tf}_2\text{N}]$ on Ag(111) – for an overview see Lexow et al.²⁸), which we have studied in the past. Since the desorption rate of $[\text{dema}][\text{TfO}]$ at RT is still very low, macroscopically thick films effectively provide a seemingly infinite reservoir on the time scale of film preparation and measurement. For ultrathin films of few multilayers thickness, however, the situation is quite different, as will be discussed below.

Growth of Ultrathin $[\text{dema}][\text{TfO}]$ Films on Ag(111) and Au(111). To study the adsorption and growth of $[\text{dema}][\text{TfO}]$, increasing amounts of the PIL were deposited onto clean Ag(111) and Au(111) surfaces by PVD, with sample temperatures of 90 K, 200 K and RT. After each experiment, the crystal surfaces were cleaned by heating above 500 K (leading to thermal desorption), Ar^+ sputtering, and annealing.

In Table 1, we summarize the quantitative analysis of a 2.6 nm thick film of $[\text{dema}][\text{TfO}]$ deposited and measured on Ag(111) at 90 K; the corresponding spectra are shown in the SI, Figure S1. The composition values for this film as derived from the 0° and 80° ARXP spectra (left values in bold) show within the accuracy of our measurements ($\pm 10\%$ for the ultrathin films, due to the low intensity of the IL signals and uncertainties in background subtraction) the same composition as that described above for the macroscopic film (italic

numbers). This clearly indicates that $[\text{dema}][\text{TfO}]$ films can be prepared on Ag(111) by PVD in UHV without decomposition during evaporation and remain intact on the surface at low temperatures. The same holds true for $[\text{dema}][\text{TfO}]$ films on Au(111) (see Figure S2 in the SI for a 2.4 nm film deposited at 200 K).

The film growth behavior can be deduced from the attenuation of the substrate signal as a function of the amount of deposited IL, using our previously established approach (for details see refs.^{28,33,35}). For perfect 2D growth, the Ag or Au signals decrease exponentially from the value I_0 for the clean surface to the value I_d for a 2D layer with thickness d , according to $I_d/I_0 = \exp(-d/(\lambda \cdot \cos \vartheta))$, with ϑ being the electron emission angle relative to surface normal. For the inelastic mean free path λ of Ag 3d electrons (kinetic energy: ~ 1100 eV), we employ 2.5 nm,^{35,41} for Au 4f electrons (kinetic energy: ~ 1400 eV), we use 3.0 nm.^{42–45}

In our analysis, we first determine the mean film thickness d from the I_d/I_0 ratio at 0° by assuming perfect 2D growth. In the next step, the I_d/I_0 ratio for this thickness at 80° is calculated, and the experimentally measured ratio is then compared to this calculated value. Agreement between the two values indicates 2D growth, and an experimental 80° value larger than the calculated one indicates a 3D morphology of the IL film.²⁸ The height h of a monolayer (1 ML) of $[\text{dema}][\text{TfO}]$ is estimated in agreement with previous publications:^{28,33} a closed film of 1 ML coverage corresponds to a bilayer of cations and anions irrespective of their relative arrangement. On the basis of the molar volume of bulk $[\text{dema}][\text{TfO}]$ ($183.6 \text{ cm}^3/\text{mol}$),⁴⁶ a closed 1 ML film has a height $h = 0.67$ nm. On the other hand, a closed single layer of ions adsorbed next to each other, with 0.5 ML coverage, has half of this height, that is, 0.34 nm. Such a film is denoted as “wetting layer” (WL) in the following.

In Figure 2a, we plot the attenuation of the Ag 3d signal at 0° and 80° emission as a function of the $[\text{dema}][\text{TfO}]$ film thickness at 90 K (blue), 200 K (red), and RT (black). The solid and dashed lines indicate the behavior for perfect 2D growth at 0° and 80° , respectively. Up to about 0.34 nm (or 0.5 ML coverage), the 80° data closely follows the prediction for 2D growth for all temperatures. This behavior indicates the formation of a closed wetting layer where the anions and cations adsorb next to each other alternatingly, that is, in a checkerboard-like structure with a saturation coverage of 0.5 ML. This adsorption behavior with both ions in direct contact with the metal surface was also observed for most AILs on metal surfaces so far.²⁸

Interestingly, at RT, the film thickness does not increase past wetting layer coverage. This behavior is attributed to the onset of multilayer desorption already below RT as will be explained in the following section in more detail. At 200 K and below, the coverage continues to increase beyond the wetting layer coverage, but while it is still decreasing, the 80° data points fall above the prediction for 2D growth. Such a behavior has been classified as “moderate” 3D island growth (that is, comparably flat 3D islands) on top of the initially formed wetting layer and is again quite commonly observed for ILs on various metal surfaces.²⁸

For the Au(111) surface, the film growth of $[\text{dema}][\text{TfO}]$ is very similar to that on Ag(111) as is evident from the attenuation of the Au 4f signal as a function of the film thickness in Figure 2b. Again, we do not observe multilayer growth at RT (black). At 200 K (red), first a closed wetting

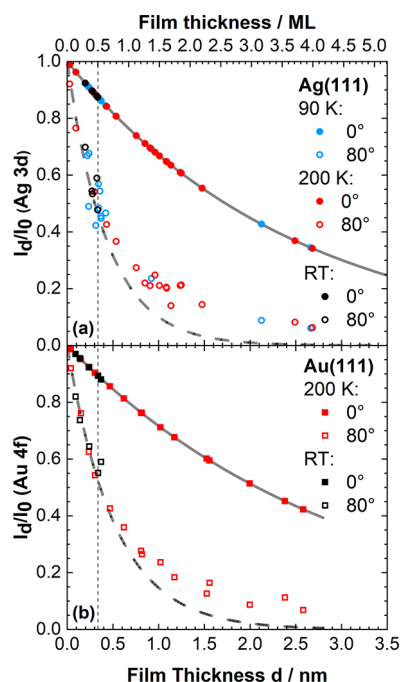


Figure 2. Dependence of the Ag 3d (circles) and Au 4f (squares) substrate signals (intensity I_d at film thickness d divided by the intensity of the uncovered surface I_0) upon deposition of [dema]-[TfO] on (a) Ag(111) and (b) Au(111), as a function of the film thickness (axis at bottom of the figure) and in units of monolayers (ML; axis at top of the figure). Data collected at 0° are shown as closed symbols and data at 80° as open symbols. The solid and dashed lines indicate the behavior for perfect 2D growth at 0° and 80° , respectively. Measurements were performed at 90 K (blue), 200 K (red), and RT (black).

layer forms, followed by similarly moderate 3D growth as on Ag(111).

[dema][TfO] Wetting Layers on Ag(111) and Au(111).

Next, we address the nature of the saturated wetting layers of [dema][TfO] on the two surfaces in detail. We start with discussing the results for Au(111), since the situation is more complex for Ag(111). In Figure 3a, C 1s, O 1s, and F 1s spectra at 0° emission of 0.5 ML on Au(111) deposited at RT are shown (note that all core level signals of the wetting layer

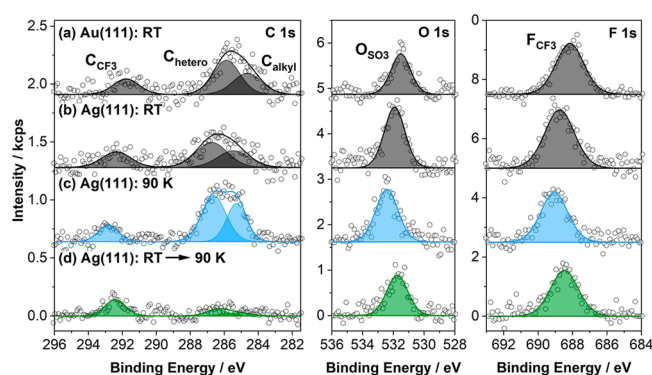


Figure 3. C 1s, O 1s, and F 1s spectra at 0° emission. (a) saturated wetting layer (= 0.5 ML) of [dema][TfO] on Au(111) deposited at RT (black); (b) saturated wetting layer of [dema][TfO] on Ag(111) deposited at RT (black); (c) 0.5 ML of [dema][TfO] on Ag(111) deposited at 90 K (blue); (d) after heating this film from 90 K to RT (green).

are shifted by about 0.4–0.7 eV toward lower binding energy with respect to the ones of the macroscopic films, which is attributed to improved final state screening by the metal in the photoemission process).⁴³ The S 2p and N 1s regions were not measured due to the low signal intensities for wetting layer coverages. The quantification of the signal intensities provides overall the nominal stoichiometry, albeit with slightly larger CF_3 -related F 1s and C 1s signals and slightly lower cationic C 1s and anionic O 1s signals (see Table 2). Quantification of the

Table 2. Composition of Layers as Obtained from Quantitative Analysis of Spectra Shown in Figure 3^a

	C_{CF_3}	C_{hetero}	C_{alkyl}	O_{SO_3}	F_{CF_3}
nominal	1	3	2	3	3
(a) Au(111): RT	1.2	2.8	1.8	2.7	3.5
(b) Ag(111): RT	1.4	2.0	1.3	3.6	4.1
(c) Ag(111): 90 K	0.9	3.0	2.0	3.1	3.0
(d) Ag(111): 90 K → RT	1.7	0.7	0.4	4.2	5.1

^a(a) Saturated wetting layer of [dema][TfO] on Au(111) deposited at RT (black); (b) saturated wetting layer layer of [dema][TfO] on Ag(111) deposited at RT (black); (c) 0.5 ML of [dema][TfO] on Ag(111) deposited at 90 K (blue); (d) after heating this film from 90 K to RT (green).

XP spectra of the [dema][TfO] wetting layer at 80° emission (not shown) reveals an even stronger attenuation of the cation-related contributions and the anion-related oxygen signal whereas anionic carbon and fluorine signals are relatively higher in intensity. This behavior indicates that the $[\text{TfO}]^-$ anion adsorbs vertically on Au(111), with the SO_3 group pointing toward and the CF_3 group away from the metal surface. Similar preferential orientation of $[\text{TfO}]^-$ anion at AIL/metal interfaces was reported previously from *in situ* IR spectroscopy studies of 1-ethyl-3-methylimidazolium trifluoromethanesulfonate ($[\text{C}_2\text{C}_1\text{Im}][\text{TfO}]$), on Pd(111)^{47–49} and on Co-covered Pd(111).⁵⁰ For the [dema]⁺ cation, our ARXPS results show no signs of preferential orientation.

The situation is different for the saturated layer of [dema][TfO] adsorbed on Ag(111) at RT as is evident from the corresponding C 1s, F 1s, and O 1s spectra in Figure 3b. Notably, we observe a strong deviation from the expected stoichiometry: while the C_{CF_3} , F_{CF_3} and O_{SO_3} signals of the anion are increased by about 30% compared to the nominal values, the cation-related C_{hetero} and C_{alkyl} signals are concomitantly decreased, which points to a considerable excess of $[\text{TfO}]^-$ in the wetting layer on Ag(111) at RT. Moreover, all absolute intensities of the anion signals are significantly higher ($35 \pm 8\%$) as compared to the saturated wetting layer on Au(111), which implies a larger amount of adsorbed anions on Ag(111): taking F 1s as the most intense anion signal for the saturated wetting layers at RT, we measure an absolute count rate of 3.4 ± 0.4 kcps for Au(111) versus 4.5 ± 0.5 kcps for Ag(111). In addition to the observed intensity changes, we also find shifts of all peaks to higher binding energy, as compared to Au(111).

To understand the observed differences, we also measured C 1s, F 1s, and O 1s spectra at 0° after depositing 0.5 ML of [dema][TfO] on Ag(111) at 90 K (Figure 3c) and after subsequent heating to RT (Figure 3d). The 0° spectra at 90 K match exactly the nominal composition indicating adsorption of intact [dema][TfO]. In particular, the observed F:O = 2.9:3.1 ratio rules out pronounced anion orientation effects at

this low temperature, where a hit-and-stick adsorption behavior has been observed for AILs.^{39,41} After heating to RT, the anion-related C 1s, F 1s, and O 1s peaks shift by about -0.5 eV to lower binding energy. More importantly, the cationic C 1s signals drastically decrease in intensity.

Since desorption of isolated cations is not possible due to energetic reasons (note that thermal evaporation of ILs only takes place in form of neutral ion pairs⁵¹), the substantial loss in cation XPS signals clearly points toward decomposition of the $[\text{dema}]^+$ cations in the wetting layer on Ag(111). As the changes in XP spectra occur during heating to RT (see also next section), we propose that the Ag(111) surface, in contrast to Au(111), enables deprotonation of the ammonium cation to form neutral diethylmethanamine ($[\text{dema}]^0$), with the latter desorbing from the surface, which leaves H^+ and $[\text{TfO}]^-$ as adsorbed trifluoromethanesulfonic acid, $\text{H}[\text{TfO}]$, behind. The observed shifts of the anion signals to lower binding energy upon heating thus might indeed be related to this cation exchange process. The remaining $[\text{TfO}]^-$ anions are well-oriented at RT with the oxygen atoms pointing toward the Ag surface and the CF_3 groups toward vacuum as shown by the F: O = 5.1:4.2 = 1.2 ratio (this ratio is similar to that of the $[\text{dema}][\text{TfO}]$ wetting layer on Au(111) at RT; see Table 2).

With this reaction in mind, our findings for the saturated wetting layer deposited on Ag(111) at RT in Figure 3b can be explained. In course of the deposition of $[\text{dema}][\text{TfO}]$ at RT, part of the $[\text{dema}]^+$ cations deprotonate and leave the surface as neutral diethylmethanamine. The liberated space allows for further $[\text{dema}][\text{TfO}]$ adsorption next to $\text{H}[\text{TfO}]$ sites, which explains the overall higher amount of $[\text{TfO}]^-$ anions mentioned above. Since we still observe notable C 1s contributions related to intact $[\text{dema}]^+$ cations in Figure 3b, the deprotonation process described above apparently leads not to a full layer of $\text{H}[\text{TfO}]$ but rather to a wetting layer consisting of $[\text{dema}][\text{TfO}]$ and $\text{H}[\text{TfO}]$ adsorbed next to each other. This also explains why the binding energies of the F 1s and O 1s peaks of the RT-deposited film in Figure 3b lie between the values for the 0.5 ML film at 90 K (Figure 3c) and the values obtained after subsequently heating this film to RT (Figure 3d).

Thermal Evolution of $[\text{dema}][\text{TfO}]$ on Au(111) and Ag(111). To investigate the desorption of $[\text{dema}][\text{TfO}]$ from Au(111), we heated a 1.5 ML film from 196 to 401 K at a heating rate of 2 K/min and simultaneously recorded Au 4f spectra of the substrate and F 1s spectra representative of the $[\text{TfO}]^-$ anion all at 0° emission (see Figure S3 in the SI). The quantitative analysis of the data is shown in Figure 4a. The intensity of anion-related F 1s signal (red) decreases in two well-separated steps while the Au 4f intensity (gray) of the Au(111) crystal increases accordingly. With reference to previous desorption studies of ILs on Ag(111) and Au(111),^{28,35,39,41} we interpret the first step with an inflection point of 292 ± 2 K as multilayer desorption of $[\text{dema}][\text{TfO}]$. From a simple leading edge-type analysis,^{28,52} we obtain an activation energy of multilayer desorption of $E_a = 101 \pm 10$ kJ/mol. This value agrees within the margins of error with the value of 91 ± 15 kJ/mol reported by Hessey et al.⁵³ with an preexponential factor of 10^{16} s^{-1} , and also with an earlier report of the enthalpy of vaporization of a structurally very similar IL, $[\text{triethylammonium}][\text{TfO}]$, of 104.9 ± 1.3 kJ/mol.⁵¹ The onset of multilayer desorption below RT provides the explanation for the absence of multilayer growth at RT described above. The remaining intensity of 3.4 ± 0.4 kcps

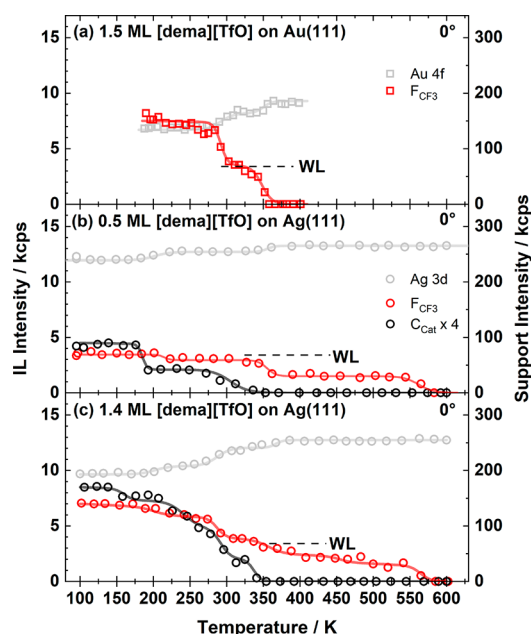


Figure 4. Thermal evolution of F 1s (red), C 1s (black), Au 4f (gray), and Ag 3d (gray) signal intensities at 0° emission upon heating films of $[\text{dema}][\text{TfO}]$ deposited at low temperature. (a) 1.5 ML on Au(111), (b) 0.5 ML on Ag(111), and (c) 1.4 ML on Ag(111). Heating rate: 2 K/min. The dashed lines indicate the nominal intensity of a saturated wetting layer (WL) of $[\text{dema}][\text{TfO}]$ as determined from XPS after direct deposition on Au(111) at RT and on Ag(111) at 90 K. The solid lines serve as guide to the eye.

between 300 and 340 K is ascribed to the wetting layer in direct contact with the Au(111) substrate and indicates its higher stability compared to the multilayers. The second desorption step at 348 ± 2 K is attributed to the desorption of the $[\text{dema}][\text{TfO}]$ wetting layer from the Au(111) surface. XPS after heating above 400 K shows no IL residuals in the F 1s, C 1s and O 1s region on Au(111). Hence we conclude that $[\text{dema}][\text{TfO}]$ desorbs intact from Au(111).

After discussing the behavior on Au(111), we address the significantly more complex thermal evolution of $[\text{dema}][\text{TfO}]$ from Ag(111) for two different initial coverages, 0.5 and 1.4 ML. The behavior of the F 1s and C 1s signals for 0.5 ML is shown in Figure 4b. This coverage corresponds to a wetting layer completely covering the surface. The anion-related F 1s intensity (red symbols) is initially constant and shows a slight decrease from ~ 3.4 to ~ 2.9 kcps at ~ 215 K. Thereafter, it stays constant up to ~ 355 K where it decreases by $\sim 50\%$ to ~ 1.5 kcps, stays constant, and finally vanishes at ~ 570 K; these intensity changes are also reflected by changes of the F 1s binding energy from 688.9 ± 0.1 eV (< 200 K) to 688.5 ± 0.3 eV and finally to 687.9 ± 0.2 eV (> 350 K); see Figure S4 in the SI. The cation-related C 1s signal (black) shows a quite different behavior, that is, it decreases to zero in two steps with inflection points at 185 ± 2 K and 305 ± 2 K. This behavior is interpreted as follows. At 185 K, roughly half of the $[\text{dema}]^+$ cations deprotonate yielding $\text{H}[\text{TfO}]$, with the neutral diethylmethanamine desorbing, which leads to the decrease of the C 1s signal. The minor step in the F 1s signals at 215 K could be a temperature-induced reorientation of the $[\text{TfO}]^-$ anion. At 305 K, the remaining $[\text{dema}]^+$ cations deprotonate yielding $\text{H}[\text{TfO}]$ and diethylmethanamine desorption. At 355 K, the formed $\text{H}[\text{TfO}]$ wetting layer partly desorbs ($\sim 50\%$),

which leads to the decrease of the F 1s signals, and partly decomposes to form a F-containing decomposition product, which is stable up to 570 K. Alternatively, 50% of H[TfO] could be stable up to 570 K, which however appears unlikely to us. Each desorption step is accompanied by a slight increase in the Ag 3d substrate signal, due to less damping by the adsorbed species. Notably, the H[TfO] desorption temperature of 355 K on Ag(111) is very similar to that of the [dema][TfO] wetting layer on Au(111).

The corresponding behavior of the 1.4 ML film is shown in Figure 4c and in Figure S5 in the SI. This coverage corresponds to a full wetting layer plus multilayers (equivalent of ~ 2 wetting layers) on top of it. The anion-related F 1s signal is constant at 6.8 ± 0.4 kcps up to 190 K, and thereafter slightly decreasing to 5.8 ± 0.4 kcps, which is accompanied by a slight increase of the Ag 3d signal. This behavior could be again due to reorganization orientation of the anions. At ~ 287 K and ~ 350 K (inflection points), the F 1s signals show small step-like decreases, which are followed by continuous decrease, until the signal disappears at 570 K. The cation-related C 1s signal again evolves independently from the anion signals. It stays more or less constant up to 215 K, apart from a slight decrease at ~ 150 K, which could be due to reorientation effects. Above 215 K, the C 1s signal decreases continuously to zero until 350 K. The behavior observed for 1.4 ML can be understood along the lines discussed for the 0.5 ML film. Starting at ~ 215 K, a fraction of the [dema]⁺ cations deprotonate yielding H[TfO] and a decrease of the C 1s signal due to diethylmethylamine desorption. This process continues up to 350 K, where the C 1s signal disappears. The step-like decrease of the F 1s signal and the simultaneous decrease of the C 1s signals at 287 K is attributed to a desorption of remaining [dema][TfO] multilayers, from the similarity of this temperature to the multilayer desorption temperature on Au(111). The small step-like decrease of the F 1s signals at ~ 350 K, where for 0.5 ML a pronounced step was seen, is attributed to the onset of the decomposition of H[TfO] to a F-containing surface species, which is stable up to 570 K.

CONCLUSIONS

The goal of this study is the detailed characterization of the adsorption, wetting, growth, and thermal evolution of protic IL [dema][TfO] films deposited onto the noble metal Au(111) and Ag(111) surfaces under well-defined UHV conditions. The quantitative analysis of several nm thick films showed the same behavior as that observed for a macroscopically thick film, which was studied as reference, confirming that [dema][TfO] remains intact upon evaporation. From angle-resolved XPS measurements, we deduce a preferential orientation of the [TfO][−] anions at the IL/vacuum interface with the CF₃ group preferentially pointing toward the vacuum side and the SO₃ groups pointing toward the bulk, in line with previous observations for aprotic ILs.

The ultrathin films of [dema][TfO] were deposited on Ag(111) and Au(111) at 90, 200, and 300 K and characterized *in situ* by ARXPS. We studied the growth behavior via the attenuation of the Ag 3d and Au 4f signals at electron emission angles of 0° and 80°. Overall, we observe a similar behavior for both surfaces. For all studied temperatures, we observe the initial growth of a closed 2D wetting layer. At RT, the film thickness does not increase past this wetting layer coverage due to multilayer desorption starting at around 290 K. Below 200

K, the coverage continues to increase, with “moderate” 3D island growth on top of the initially formed wetting layer.

On Au(111), [dema][TfO] is stable at RT. In contrast, on the more reactive Ag(111) surface, the [dema]⁺ cations partly deprotonate well below RT yielding H[TfO] and neutral diethylmethylamine [dema]⁰. The formed amine is volatile and desorbs instantaneously leaving a mixture of H[TfO] and [dema][TfO] on the surface. Consequently, a higher coverage of [TfO][−] is achieved than on Au(111) due to the smaller size of H⁺ as compared to [dema]⁺. When adsorbing a WL of [dema][TfO] on Ag(111) at 90 K and subsequently heating to RT, nearly all [dema][TfO] is deprotonated to H[TfO]. The larger amount of intact [dema][TfO] observed for adsorption at RT in comparison to the amount obtained after adsorption at 90 K plus heating to RT is attributed to further adsorption of intact [dema][TfO] at free adsorption sites after desorption of [dema]⁰.

Further insight was obtained by following the thermal evolution *in situ* during heating, after deposition at low temperature. On Au(111), we deposited 1.5 ML [dema][TfO] at 200 K and subsequently heated it to 400 K. We observe the desorption of the [dema][TfO] multilayer at 292 K, leaving an intact [dema][TfO] wetting layer on Au(111). The onset of multilayer desorption below RT is the reason for the absence of multilayer growth at RT. The wetting layer desorbs intact at 348 K leaving a clean Au(111) surface above 400 K.

The behavior on Ag(111) is much more complex. Upon heating a [dema][TfO] wetting layer (0.5 ML) deposited at 90 K, we observe that the [dema]⁺ cations deprotonate in two steps at 185 and 305 K, yielding H[TfO] and volatile [dema]⁰. At 355 K, the formed H[TfO] wetting layer partly desorbs ($\sim 50\%$) and partly decomposes forming a F-containing surface species, which is stable up to 570 K. The behavior observed for a 1.4 ML [dema][TfO] film deposited at 90 K and heated up to 600 K can be understood along the deprotonation effects at the Ag-PIL interface as found in the wetting layer film superimposed by the multilayer signals.

All in all, our results demonstrate a rather complex behavior of this protic IL in contact with the moderately reactive Ag(111) surface even well below room temperature. The discussed deprotonation effects should thus be taken into consideration in all situations where PIL/solid interfaces are present such as in electrochemistry, nanoparticle formation, and many more, particularly, when more reactive metals than silver are involved.

EXPERIMENTAL SECTION

The synthesis and characterization of [dema][TfO] was described in ref 54. After careful degassing in UHV, it was deposited onto Au(111) and Ag(111) via physical vapor deposition (PVD) in UHV from a modified Knudsen cell with a boron nitride crucible at a temperature between 343 and 353 K, which provides a very stable IL flux; the details of the Knudsen cell have been published in ref 41. The PIL flux was monitored with a quartz crystal microbalance before and after deposition to ensure a constant evaporation rate. We found no signs of decomposition of [dema][TfO] in our quantitative XPS analysis of multilayer films from PVD on Ag(111) at 90 K and Au(111) at 200 K. This behavior is in line with literature reports, where decomposition of bulk [dema][TfO] is only found at temperatures above 633 K.¹⁰ Furthermore, it agrees also with more recent observations for a similar PIL, [triethylammonium][TfO], which has been shown to evaporate as ion pairs.^{51,55}

The Ag(111) and Au(111) single crystals with circular shapes were purchased from MaTeck (15 mm in diameter, purity 99.999%,

polished with an alignment better than 0.1° to the (111) plane). They were cleaned in UHV by short heating to >500 K and subsequent Ar^+ sputtering (600 V, 8 μA) for 30 min at RT, followed by an annealing step at 800 K for 10 min. The surface temperature was measured using type-K thermocouple wires inserted into a 0.5 mm pinhole of the crystal with an absolute accuracy of ± 20 K (at 500 K) and a reproducibility of ± 2 K.

The UHV system for angle-resolved X-ray photoelectron spectroscopy (ARXPS) contains a nonmonochromated Al $K\alpha$ X-ray source (SPECS XR 50, 1486.6 eV, 240 W) and a hemispherical electron analyzer (VG SCIENTA R3000) (described in more detail in ref 35). A pass energy of 100 eV was applied for all spectra leading to an overall energy resolution of about 0.9 eV.³⁵ The spectra were quantitatively evaluated in CasaXPS V2.3.16Dev6. Shirley backgrounds⁵⁶ were subtracted for Ag 3d and Au 4f core levels. For the F 1s, C 1s, O 1s, S 2p, and N 1s regions, linear backgrounds were subtracted and then peaks were fitted with Voigt profiles (30% Lorentzian contribution). The binding energy scale for XPS of the macroscopic films of [dema][TfO] was calibrated such that the F_{CF_3} peak is located at 688.5 eV.^{30–32} The spectra of thin films of the ILs of Ag(111) and Au(111) were referenced to the Fermi edge yielding 368.20 eV for the Ag $3d_{5/2}$ level and 83.85 eV for the Au $4f_{7/2}$ level. In agreement with literature,^{31,32} we fitted the C 1s components related to the [dema]⁺ cation with two contributions: C_{hetero} for the three carbon atoms directly bonded to the nitrogen atom and C_{alkyl} for the two alkyl carbon atoms further away from the central nitrogen atom. For the measurements of the wetting layer in 0° emission, we applied a constraint to the peak areas of $\text{C}_{\text{hetero}}/\text{C}_{\text{alkyl}} = 3:2$. Additionally, we subtracted a residual carbon contamination signal that could not be removed even after repeated cleaning cycles from both surfaces. In case of Ag(111), we also subtracted the K_β satellite of the Ag 3d signal above 296 eV. Temperature-programmed XPS was measured at a heating rate of 2 K/min.

■ ASSOCIATED CONTENT

Supporting Information

The Supporting Information is available free of charge at <https://pubs.acs.org/doi/10.1021/acs.langmuir.1c01823>.

Additional XPS spectra addressing the chemical composition and thermal evolution of ultrathin [dema]-[TfO] films (PDF)

■ AUTHOR INFORMATION

Corresponding Author

Hans-Peter Steinrück – Lehrstuhl für Physikalische Chemie 2, Friedrich-Alexander-Universität Erlangen-Nürnberg, 91058 Erlangen, Germany; orcid.org/0000-0003-1347-8962; Email: hans-peter.steinrueck@fau.de

Authors

Stephen Massicot – Lehrstuhl für Physikalische Chemie 2, Friedrich-Alexander-Universität Erlangen-Nürnberg, 91058 Erlangen, Germany; orcid.org/0000-0002-2530-8015

Tomoya Sasaki – Department of Applied Chemistry, Graduate School of Engineering, Osaka University, Suita, Osaka 565-0871, Japan; orcid.org/0000-0001-5503-5823

Matthias Lexow – Lehrstuhl für Physikalische Chemie 2, Friedrich-Alexander-Universität Erlangen-Nürnberg, 91058 Erlangen, Germany; orcid.org/0000-0002-1441-2909

Sunghwan Shin – Lehrstuhl für Physikalische Chemie 2, Friedrich-Alexander-Universität Erlangen-Nürnberg, 91058 Erlangen, Germany

Florian Maier – Lehrstuhl für Physikalische Chemie 2, Friedrich-Alexander-Universität Erlangen-Nürnberg, 91058 Erlangen, Germany; orcid.org/0000-0001-9725-8961

Susumu Kuwabata – Department of Applied Chemistry, Graduate School of Engineering, Osaka University, Suita, Osaka 565-0871, Japan; orcid.org/0000-0002-4606-964X

Complete contact information is available at: <https://pubs.acs.org/doi/10.1021/acs.langmuir.1c01823>

Notes

The authors declare no competing financial interest.

■ ACKNOWLEDGMENTS

H.-P.S. and M.L. thank the European Research Council (ERC) for support through the Advanced Investigator Grant “ILID” to H.-P.S. (grant agreement no. 693398-ILID) under the European Union’s Horizon 2020 research and innovation programme. S. S. thanks the Alexander von Humboldt Foundation for a research fellowship. S.M. was funded by the Deutsche Forschungsgemeinschaft (DFG, German Research Foundation) – Project-ID 431791331 – SFB 1452.

■ REFERENCES

- (1) Greaves, T. L.; Drummond, C. J. Protic Ionic Liquids: Properties and Applications. *Chem. Rev.* **2008**, *108*, 206–237.
- (2) Brzeczek-Szafran, A.; Wieclawik, J.; Barteczko, N.; Szelwicka, A.; Byrne, E.; Kolanowska, A.; Swadźba Kwaśny, M.; Chrobok, A. Protic Ionic Liquids from Di- or Triamines: Even Cheaper Brønsted Acidic Catalysts. *Green Chem.* **2021**, *23*, 4421–4429.
- (3) Chen, L.; Sharifzadeh, M.; Mac Dowell, N.; Welton, T.; Shah, N.; Hallett, J. P. Inexpensive Ionic Liquids: $[\text{HSO}_4]$ -Based Solvent Production at Bulk Scale. *Green Chem.* **2014**, *16*, 3098–3106.
- (4) Greaves, T. L.; Drummond, C. J. Protic Ionic Liquids: Evolving Structure-Property Relationships and Expanding Applications. *Chem. Rev.* **2015**, *115*, 11379–11448.
- (5) Lee, S.-Y.; Ogawa, A.; Kanno, M.; Nakamoto, H.; Yasuda, T.; Watanabe, M. Nonhumidified Intermediate Temperature Fuel Cells Using Protic Ionic Liquids. *J. Am. Chem. Soc.* **2010**, *132*, 9764–9773.
- (6) Pourcelly, G. Membranes for Low and Medium Temperature Fuel Cells. State-of-the-Art and New Trends. *Pet. Chem.* **2011**, *51*, 480–491.
- (7) Yoshizawa, M.; Xu, W.; Angell, C. A. Ionic Liquids by Proton Transfer: Vapor Pressure, Conductivity, and the Relevance of Δp_{ka} from Aqueous Solutions. *J. Am. Chem. Soc.* **2003**, *125*, 15411–15419.
- (8) Hallett, J. P.; Welton, T. Room-Temperature Ionic Liquids: Solvents for Synthesis and Catalysis. 2. *Chem. Rev.* **2011**, *111*, 3508–3576.
- (9) Yasuda, T.; Watanabe, M. Protic Ionic Liquids: Fuel Cell Applications. *MRS Bull.* **2013**, *38*, 560–566.
- (10) Nakamoto, H.; Watanabe, M. Brønsted Acid-Base Ionic Liquids for Fuel Cell Electrolytes. *Chem. Commun.* **2007**, 2539–2541.
- (11) Lovelock, K. R. J. Quantifying Intermolecular Interactions of Ionic Liquids Using Cohesive Energy Densities. *R. Soc. Open Sci.* **2017**, *4*, 171223.
- (12) Esperança, J. M. S. S.; Canongia Lopes, J. N.; Tariq, M.; Santos, L. M. N. B. F.; Magee, J. W.; Rebelo, L. P. N. Volatility of Aprotic Ionic Liquids — a Review. *J. Chem. Eng. Data* **2010**, *55*, 3–12.
- (13) Lovelock, K. R. J. Influence of the Ionic Liquid/Gas Surface on Ionic Liquid Chemistry. *Phys. Chem. Chem. Phys.* **2012**, *14*, 5071–5089.
- (14) Yu, H.; Dyett, B. P.; Pathirannahalage, S. K.; Li, M.; Drummond, C. J.; Greaves, T. L. Formation of Surface Protic Ionic Liquid Nanodroplets for Nanofabrication. *Adv. Mater. Interfaces* **2020**, *7*, 1901647.
- (15) Johnson, L.; Ejigu, A.; Licence, P.; Walsh, D. A. Hydrogen Oxidation and Oxygen Reduction at Platinum in Protic Ionic Liquids. *J. Phys. Chem. C* **2012**, *116*, 18048–18056.

- (16) Ejigu, A.; Johnson, L.; Licence, P.; Walsh, D. A. Electrocatalytic Oxidation of Methanol and Carbon Monoxide at Platinum in Protic Ionic Liquids. *Electrochem. Commun.* **2012**, *23*, 122–124.
- (17) Ingale, P.; Sakthivel, M.; Drillet, J. F. Test of Diethylmethylammonium Trifluoromethanesulfonate Ionic Liquid as Electrolyte in Electrically Rechargeable Zn/Air Battery. *J. Electrochem. Soc.* **2017**, *164*, H5224–H5229.
- (18) Meng, T.; Young, K.-H.; Wong, D. F.; Nei, J. Ionic Liquid-Based Non-Aqueous Electrolytes for Nickel/Metal Hydride Batteries. *Batteries* **2017**, *3*, 4.
- (19) George, A.; et al. Design of Low-Cost Ionic Liquids for Lignocellulosic Biomass Pretreatment. *Green Chem.* **2015**, *17*, 1728–1734.
- (20) Verdía, P.; Brandt, A.; Hallett, J. P.; Ray, M. J.; Welton, T. Fractionation of Lignocellulosic Biomass with the Ionic Liquid 1-Butylimidazolium Hydrogen Sulfate. *Green Chem.* **2014**, *16*, 1617–1627.
- (21) Pająk, M.; Hubkowska, K.; Czerwiński, A. The Study of Hydrogen Sorption in Palladium Limited Volume Electrode from Dema-Tfo Ionic Liquid. *J. Electroanal. Chem.* **2018**, *825*, 73–76.
- (22) Hamm, S. C.; et al. Sputter-Deposition of Silver Nanoparticles into Ionic Liquid as a Sacrificial Reservoir in Antimicrobial Organosilicate Nanocomposite Coatings. *ACS Appl. Mater. Interfaces* **2012**, *4*, 178–184.
- (23) Bhujbal, A. V.; Raut, A. B.; Bhanage, B. M. Water-Assisted Electrochemical Fabrication of Cu/Cu₂O Nanoparticles in Protic Ionic Liquid and Their Catalytic Activity in the Synthesis of Quinazolinones. *React. Kinet., Mech. Catal.* **2020**, *131*, 905.
- (24) Izumi, R.; Yao, Y.; Tsuda, T.; Torimoto, T.; Kuwabata, S. Pt-Nanoparticle-Supported Carbon Electrocatalysts Functionalized with a Protic Ionic Liquid and Organic Salt. *Adv. Mater. Interfaces* **2018**, *5*, 1701123.
- (25) Sasaki, T.; Uematsu, T.; Tsuda, T.; Kuwabata, S. Operando Observation of Vacuum and Liquid Interface While Conducting Gold Sputtering onto Ionic Liquid for Preparation of Au Nanoparticles. *Electrochemistry* **2018**, *86*, 223–225.
- (26) Tsuda, T.; Kurihara, T.; Hoshino, Y.; Kiyama, T.; Okazaki, K.-i.; Torimoto, T.; Kuwabata, S. Electrocatalytic Activity of Platinum Nanoparticles Synthesized by Room-Temperature Ionic Liquid-Sputtering Method. *Electrochemistry* **2009**, *77*, 693–695.
- (27) Yoshii, K.; Tsuda, T.; Arimura, T.; Imanishi, A.; Torimoto, T.; Kuwabata, S. Platinum Nanoparticle Immobilization onto Carbon Nanotubes Using Pt-Sputtered Room-Temperature Ionic Liquid. *RSC Adv.* **2012**, *2*, 8262–8264.
- (28) Lexow, M.; Maier, F.; Steinrück, H.-P. Ultrathin Ionic Liquid Films on Metal Surfaces: Adsorption, Growth, Stability and Exchange Phenomena. *Advances in Physics: X* **2020**, *5*, 1761266.
- (29) Miran, M. S.; Kinoshita, H.; Yasuda, T.; Susan, M. A. B. H.; Watanabe, M. Physicochemical Properties Determined by Δp_K for Protic Ionic Liquids Based on an Organic Super-Strong Base with Various Brønsted Acids. *Phys. Chem. Chem. Phys.* **2012**, *14*, 5178–5186.
- (30) Fogarty, R. M.; Matthews, R. P.; Ashworth, C. R.; Brandt-Talbot, A.; Palgrave, R. G.; Bourne, R. A.; Hoogerstraete, T. V.; Hunt, P. A.; Lovelock, K. R. J. Experimental Validation of Calculated Atomic Charges in Ionic Liquids. *J. Chem. Phys.* **2018**, *148*, 193817.
- (31) Fogarty, R. M.; Palgrave, R. G.; Bourne, R. A.; Handrup, K.; Villar-García, I. J.; Payne, D. J.; Hunt, P. A.; Lovelock, K. R. J. Electron Spectroscopy of Ionic Liquids: Experimental Identification of Atomic Orbital Contributions to Valence Electronic Structure. *Phys. Chem. Chem. Phys.* **2019**, *21*, 18893–18910.
- (32) Fogarty, R. M.; Rowe, R.; Matthews, R. P.; Clough, M. T.; Ashworth, C. R.; Brandt, A.; Corbett, P. J.; Palgrave, R. G.; Smith, E. F.; Bourne, R. A.; Chamberlain, T. W.; Thompson, P. B. J.; Hunt, P. A.; Lovelock, K. R. J.; et al. Atomic Charges of Sulfur in Ionic Liquids: Experiments and Calculations. *Faraday Discuss.* **2018**, *206*, 183–201.
- (33) Cremer, T.; Killian, M.; Gottfried, J. M.; Paape, N.; Wasserscheid, P.; Maier, F.; Steinrück, H.-P. Physical Vapor Deposition of [Emim][Tf₂n]: A New Approach to the Modification of Surface Properties with Ultrathin Ionic Liquid Films. *ChemPhysChem* **2008**, *9*, 2185–2190.
- (34) Steinrück, H.-P. Recent Developments in the Study of Ionic Liquid Interfaces Using X-Ray Photoelectron Spectroscopy and Potential Future Directions. *Phys. Chem. Chem. Phys.* **2012**, *14*, 5010–5029.
- (35) Lexow, M.; Talwar, T.; Heller, B. S. J.; May, B.; Bhui, R. G.; Maier, F.; Steinrück, H.-P. Time-Dependent Changes in the Growth of Ultrathin Ionic Liquid Films on Ag(111). *Phys. Chem. Chem. Phys.* **2018**, *20*, 12929–12938.
- (36) Wittstock, A.; et al. Nanoporous Au: An Unsupported Pure Gold Catalyst? *J. Phys. Chem. C* **2009**, *113*, 5593–5600.
- (37) Xu, B.; Siler, C.; Madix, R.; Friend, C., Ag/Au Mixed Sites Promote Oxidative Coupling of Methanol on the Alloy Surface. *Chem. - Eur. J.* **2014**, *20*, 4646.
- (38) Maier, F.; Cremer, T.; Kolbeck, C.; Lovelock, K. R. J.; Paape, N.; Schulz, P. S.; Wasserscheid, P.; Steinrück, H. P. Insights into the Surface Composition and Enrichment Effects of Ionic Liquids and Ionic Liquid Mixtures. *Phys. Chem. Chem. Phys.* **2010**, *12*, 1905–1915.
- (39) Lexow, M.; Heller, B. S. J.; Partl, G.; Bhui, R. G.; Maier, F.; Steinrück, H.-P. Cation Exchange at the Interfaces of Ultrathin Films of Fluorous Ionic Liquids on Ag(111). *Langmuir* **2019**, *35*, 398–405.
- (40) Heller, B.; Lexow, M.; Greco, F.; Shin, S.; Partl, G. J.; Maier, F.; Steinrück, H.-P., Temperature-Dependent Surface Enrichment Effects in Binary Mixtures of Fluorinated and Non-Fluorinated Ionic Liquids. *Chem. - Eur. J.* **2020**, *26*, 1117.
- (41) Lexow, M.; Heller, B. S. J.; Maier, F.; Steinrück, H.-P. Anion Exchange at the Liquid/Solid Interface of Ultrathin Ionic Liquid Films on Ag(111). *ChemPhysChem* **2018**, *19*, 2978–2984.
- (42) Rietzler, F.; May, B.; Steinrück, H. P.; Maier, F. Switching Adsorption and Growth Behavior of Ultrathin [C₂C₁Im][Otf] Films on Au(111) by Pd Deposition. *Phys. Chem. Chem. Phys.* **2016**, *18*, 25143–25150.
- (43) Cremer, T.; Stark, M.; Deyko, A.; Steinrück, H. P.; Maier, F. Liquid/Solid Interface of Ultrathin Ionic Liquid Films: [C₁C₁Im]-[Tf₂N] and [C₈C₁Im][Tf₂N] on Au(111). *Langmuir* **2011**, *27*, 3662–3671.
- (44) Deyko, A.; Bajus, S.; Rietzler, F.; Bösmann, A.; Wasserscheid, P.; Steinrück, H.-P.; Maier, F. Interface Properties and Physicochemical Characterization of the Low-Temperature Molten Salt Li/K/Cs Acetate. *J. Phys. Chem. C* **2013**, *117*, 22939–22946.
- (45) Rietzler, F.; Piermaier, M.; Deyko, A.; Steinrück, H.-P.; Maier, F. Electrospray Ionization Deposition of Ultrathin Ionic Liquid Films: [C₈C₁Im]Cl and [C₈C₁Im][Tf₂N] on Au(111). *Langmuir* **2014**, *30*, 1063–1071.
- (46) Atilhan, M.; Anaya, B.; Ullah, R.; Costa, L. T.; Aparicio, S. Double Salt Ionic Liquids Based on Ammonium Cations and Their Application for CO₂ Capture. *J. Phys. Chem. C* **2016**, *120*, 17829–17844.
- (47) Bauer, T.; Mehl, S.; Brummel, O.; Pohako-Esko, K.; Wasserscheid, P.; Libuda, J. Ligand Effects at Ionic Liquid-Modified Interfaces: Coadsorption of [C₂C₁Im][Otf] and Co on Pd(111). *J. Phys. Chem. C* **2016**, *120*, 4453–4465.
- (48) Schernich, S.; Kostyshyn, D.; Wagner, V.; Taccardi, N.; Laurin, M.; Wasserscheid, P.; Libuda, J. Interactions between the Room-Temperature Ionic Liquid [C₂C₁Im][Otf] and Pd(111), Well-Ordered Al₂O₃, and Supported Pd Model Catalysts from Ir Spectroscopy. *J. Phys. Chem. C* **2014**, *118*, 3188–3193.
- (49) Schernich, S.; Wagner, V.; Taccardi, N.; Wasserscheid, P.; Laurin, M.; Libuda, J. Interface Controls Spontaneous Crystallization in Thin Films of the Ionic Liquid [C₂C₁Im][Otf] on Atomically Clean Pd(111). *Langmuir* **2014**, *30*, 6846–6851.
- (50) Mehl, S.; Bauer, T.; Brummel, O.; Pohako-Esko, K.; Schulz, P.; Wasserscheid, P.; Libuda, J. Ionic-Liquid-Modified Hybrid Materials Prepared by Physical Vapor Codeposition: Cobalt and Cobalt Oxide Nanoparticles in [C₁C₂Im][Otf] Monitored by in Situ Ir Spectroscopy. *Langmuir* **2016**, *32*, 8613–8622.
- (51) Zaitsau, D. H.; Emel'yanenko, V. N.; Stange, P.; Verevkin, S. P.; Ludwig, R. Dissecting the Vaporization Enthalpies of Ionic Liquids by

Exclusively Experimental Methods: Coulomb Interaction, Hydrogen Bonding, and Dispersion Forces. *Angew. Chem., Int. Ed.* **2019**, *58*, 8589–8592.

(52) Lexow, M.; Massicot, S.; Maier, F.; Steinrück, H.-P. Stability and Exchange Processes in Ionic Liquid/Porphyrin Composite Films on Metal Surfaces. *J. Phys. Chem. C* **2019**, *123*, 29708–29721.

(53) Hessey, S.; Jones, R. On the Evaporation, Bonding, and Adsorbate Capture of an Ionic Liquid on Au(111). *Chem. Sci.* **2013**, *4*, 2519–2529.

(54) Sasaki, T.; Inoue, S.; Kuwabata, S. Room-Temperature Fabrication of Electrocatalyst for Oxygen Reduction Using Pt Nanoparticle-Dispersed Protic Ionic Liquid with Poly(3,4-Ethylenedioxythiophene). *Electrochemistry* **2021**, *89*, 83–86.

(55) Horikawa, M.; Akai, N.; Kawai, A.; Shibuya, K. Vaporization of Protic Ionic Liquids Studied by Matrix-Isolation Fourier Transform Infrared Spectroscopy. *J. Phys. Chem. A* **2014**, *118*, 3280–3287.

(56) Shirley, D. A. High-Resolution X-Ray Photoemission Spectrum of the Valence Bands of Gold. *Phys. Rev. B* **1972**, *5*, 4709–4714.